Chemical Science

ROYAL SOCIETY OF CHEMISTRY

EDGE ARTICLE

View Article Online
View Journal | View Issue

Cite this: *Chem. Sci.*, 2024, **15**, 12957

All publication charges for this article have been paid for by the Royal Society of Chemistry

Received 13th March 2024
Accepted 8th July 2024

DOI: 10.1039/d4sc01721h

rsc.li/chemical-science

Structural modulation of aggregation-induced emission luminogens for NIR-II fluorescence imaging/photoacoustic imaging of tumors†

Xue Liu,‡[a] Yonghong Tan,‡[a] Jianyu Zhang,‡[c] Weigeng Huang,[a] Dingyuan Yan,*[a] Dong Wang*[a] and Ben Zhong Tang*[bc]

Concurrent near-infrared-II (NIR-II) fluorescence imaging (FLI) and photoacoustic imaging (PAI) holds tremendous potential for effective disease diagnosis owing to their combined benefits and complementary features, in particular on the basis of a single molecule. However, the simultaneous guarantee of high-quality NIR-II FLI and PAI is recognized to be challenging impeded by the competitive photophysical processes at the molecular level. Herein, a simple organic fluorophore, namely T-NSD, is finely engineered with facile synthetic procedures through delicately modulating the rigidity and electron-withdrawing ability of the molecular acceptor. The notable advantages of fabricated T-NSD nanoparticles include a large Stokes shift, intense fluorescence emission in the NIR-II region, and anti-quenching properties in the aggregated states, which eventually enable the implementation of dual-modal NIR-II FLI/PAI in a 4T1 tumor-xenografted mouse model with reliable performance and good biocompatibility. Overall, these findings present a simple strategy for the construction of NIR-II optical agents to allow multimodal disease diagnosis.

1 Introduction

Optical imaging possesses distinct superiorities such as nonionizing and noninvasive features, exceptional spatiotemporal resolution, and enabling the implementation of multiple imaging, thereby facilitating disease diagnosis and treatment across a wide range of applications from subcellular *in vitro* studies to *in vivo* investigations.[1–3] Among the various optical imaging techniques, fluorescence imaging (FLI) in the second near-infrared (NIR-II, 1000–1700 nm) window has gained extensive attention in the past two decades due to its high signal-to-noise ratio, high sensitivity, optimal tissue penetration depth.[4–7] Despite the aforementioned advantages, the limited penetration depth (~1 cm) continues to be regarded as its Achilles' heel which severely hinders its further advancement.[8] Photoacoustic imaging (PAI), an emerging modality that integrates optical and ultrasound imaging, is capable of offering a tissue penetration depth of up to 5 cm.[9–11] Nevertheless, it is confronted with shortcomings in terms of sensitivity and feedback speed. Under these circumstances, the integration of NIR-II FLI and PAI can perfectly compensate for the deficiencies inherent in each modality and thus provide more comprehensive diagnostic details compared with single-modal imaging.[12–15]

Organic optical agents, particularly small molecules, are preferred on account of their accessibility to multi-functionalities by strategic molecular engineering, thus permitting synchronized NIR-II FLI and PAI capacities.[16] Additionally, considering translational potentiality, small organic agents may have greater promise due to their well-defined compositions and excellent biodegradability.[17,18] Due to their intrinsic hydrophobicity, most NIR-II fluorophores require to be fabricated into nanoparticles (NPs) for bio-applications.[19] However, conventional NIR-II fluorophores with a planar conformation may encounter the issue of aggregation-caused quenching ascribed to the undesirable intermolecular π–π stacking in the nanoaggregates.[20] Thanks to the emergence of aggregation-induced emission luminogens (AIEgens), the dilemma of reduced FLI in the aggregated state is effectively resolved based on the mechanism of restriction of intramolecular motion.[21–23] Moreover, the unique twisted backbone

[a]*Center for AIE Research, Shenzhen Key Laboratory of Polymer Science and Technology, Guangdong Research Center for Interfacial Engineering of Functional Materials, College of Materials Science and Engineering, Shenzhen University, Shenzhen 518060, China. E-mail: yandingyuan@szu.edu.cn; wangd@szu.edu.cn*

[b]*School of Science and Engineering, Shenzhen Institute of Aggregate Science and Technology, The Chinese University of Hong Kong, Shenzhen (CUHK-Shenzhen), Guangdong 518172, China. E-mail: tangbenz@cuhk.edu.cn*

[c]*Hong Kong Branch of Chinese National Engineering Research Center for Tissue Restoration and Reconstruction, Department of Chemistry, State Key Laboratory of Neuroscience, Department of Chemical and Biomedical Engineering, The Hong Kong University of Science and Technology, Kowloon, Hong Kong 999077, China*

† Electronic supplementary information (ESI) available: Synthesis of the probes, ^{1}H NMR spectrum of the probes, ^{13}C NMR spectrum of the probes. See DOI: https://doi.org/10.1039/d4sc01721h

‡ X. Liu, Y. Tan and J. Zhang contributed equally to this work.

of AIEgens is beneficial to promote the intense motion of rotors/vibrators, which is the prerequisite for attaining high-quality PAI.[24,25] Therefore, multimodal diagnosis based on the versatile NIR-II AIEgens has met with a splendid phase of development in the past five years.[26–28] Despite significant advancements, these compounds are typically featured with a large conjugated skeleton that necessitates laborious synthetic procedures due to the scarcity of novel design philosophy.

Herein, a new NIR-II AIEgen, namely T-NSD, has been elaborately prepared by modulating the molecular steric hindrance and enhancing the electronic donating–accepting interaction (Scheme 1A). Benefiting from the and strengthened electron-withdrawing capacity of the central naphtho[2,3-*c*][1,2,5]selenadiazole (NSD) moiety, T-NSD exhibits obvious AIE attributes with intense fluorescence emission in the NIR-II window. To the best of our knowledge, T-NSD possesses the simplest structural skeleton and the shortest synthetic steps among all reported NIR-II AIEgens. After being encapsulated by 1,2-distearoyl-*sn*-glycero-3-phosphoethanolamine-*N*-[methoxy(polyethylene glycol)-2000] (DSPE-mPEG$_{2000}$), T-NSD nanoparticles (NPs) were prepared with exceptional cellular uptake efficiency and good biocompatibility. Eventually, bimodal NIR-II FLI/PAI of subcutaneous tumors in a 4T1 tumor-xenografted mouse model was carried out under the irradiation of a 660 nm laser (Scheme 1B). The present study proposes a simple tactic for the design of NIR-II AIEgens that can be employed for disease diagnosis under integrated imaging modalities.

2 Results

2.1 Design, synthesis and optical property investigations

Taking the salient advantages of abundant availability and electron-rich features, thiophene derivatives have been widely adopted as π-bridges in the synthesis of organic photoelectric materials.[29] Initially, thiophene was recommended as a π-bridge to connect di-*p*-tolylamine and commercial available benzo[1,2,5]thiadiazole (BTD) to obtain T-BTD (Fig. 1A and Scheme S1†). To enhance the electron donor (D)–acceptor (A) interactions, naphtho[2,3-*c*][1,2,5]thiadiazole (NTD) was chosen to generate T-NTD. As shown in Fig. 1B, the dihedral angles between thiophene and A significantly increased from 13.9° to ~50° in the ground-state (S_0) when BTD was replaced by NTD, which can be ascribed to the increased spatial hindrance between the thiophene unit and NTD. The incorporation of a highly electron-withdrawing central naphtho[2,3-*c*][1,2,5] selenadiazole (NSD) core can further lower the energy bandgap of the resulting T-NSD.[30] All the key intermediates and final products were thoroughly confirmed by using nuclear magnetic resonance and mass spectra (Fig. S1–S11, ESI†). The energy

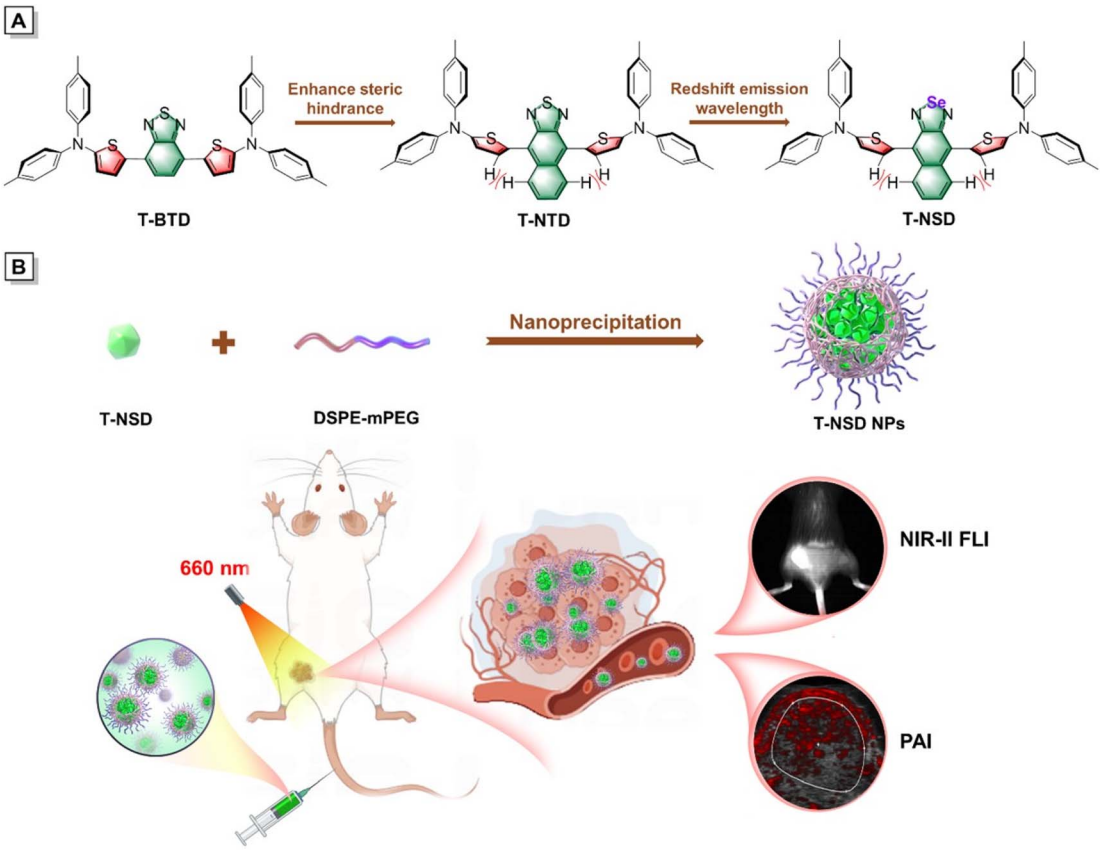

Scheme 1 Preparation of NIR-II AIE nanoparticles for tumor diagnosis. (A) Molecular design philosophy by modulating the rigidity and electron-withdrawing ability of the molecular acceptor. (B) Illustration of the fabrication of T-NSD nanoparticles and their application in dual-modal NIR-II FLI/PAI of tumors.

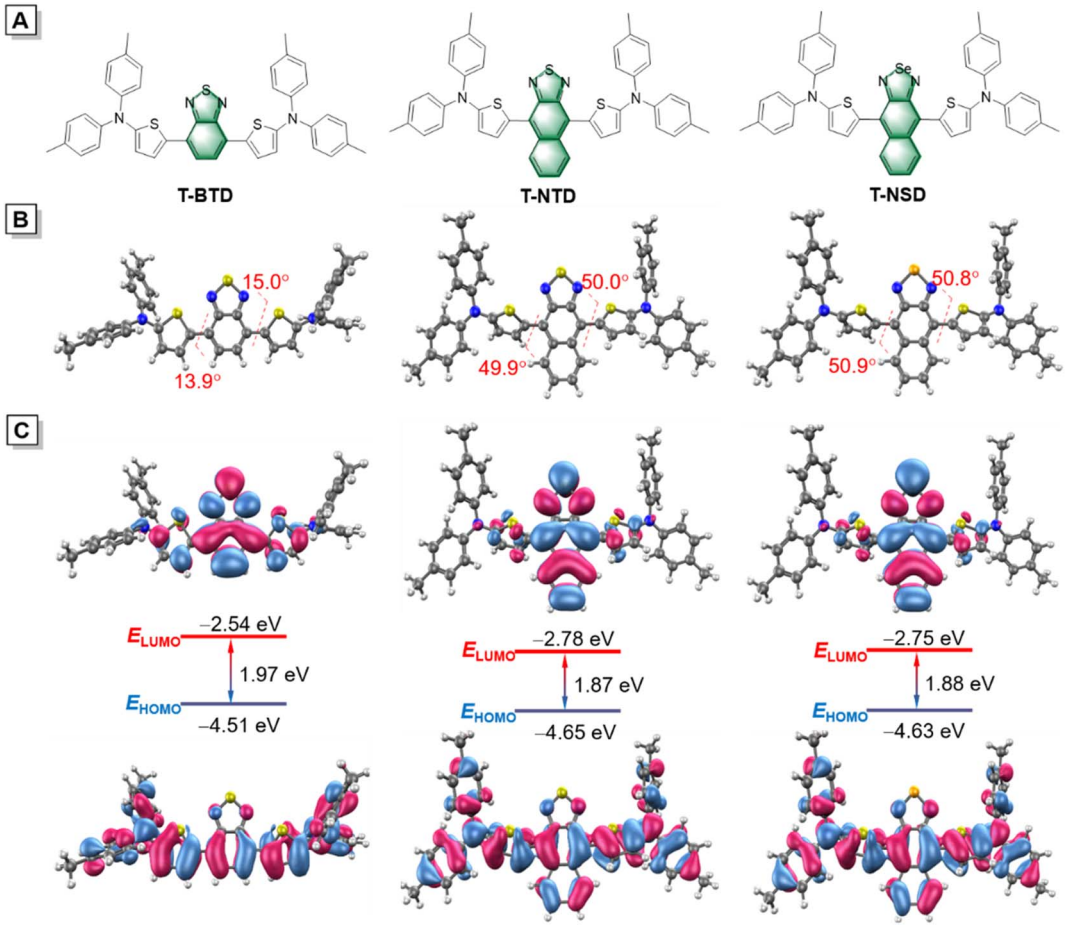

Fig. 1 Structure details of T-BTD, T-NTD and T-NSD. (A) Chemical structures, (B) optimized S_0 geometries and (C) illustration of the frontier molecular orbitals (LUMOs and HOMOs) determined at the M06-2X/6-31G(d,p) level of theory, using the Gaussian 16 program.

bandgaps of T-TD, T-NTD, and T-NSD were calculated to be 1.97 eV, 1.87 eV, and 1.88 eV respectively based on the highest occupied molecular orbital (HOMO) and lowest unoccupied molecular orbital (LUMO) levels of the molecules, confirming the successful manipulation of absorption/emission wavelengths towards longer ranges (Fig. 1C).

The optical properties of these three compounds were then systematically investigated. As depicted in Fig. 2A, the maximum absorption peaks of T-BTD, T-NTD, and T-NSD in THF solution are located at 563 nm, 615 nm and 660 nm, respectively. Correspondingly, their maximum emission wavelengths exhibited a similar red shifting trend well consistent with their absorptions (Fig. 2B). Notably, T-NSD exhibited a wide emission spectrum with a peak at around 1000 nm, manifesting its capability for performing NIR-II FLI. Subsequently, their AIE properties were evaluated by recording the fluorescence emission spectra in a THF/water binary solution system with varying water fractions (f_w). As shown in Fig. 2C and S12 (ESI),† T-BTD displayed weak AIE characteristics as f_w gradually varied from 0 to 90%. However, the incorporation of bulky NTD or an NSD central core led to a pronounced torsion of the molecular backbone, thereby contributing to the enhancement of the AIE signature. We then conducted calculations to probe the energy dissipation pathway of three luminogens upon excitation. The total reorganization energies of T-BTD, T-NTD, and T-NSD were calculated to be 3237 cm^{-1}, 3866 cm^{-1}, and 4950 cm^{-1}, respectively by using the Molecular Materials Property Prediction Package (MOMAP) program.[31–33] Specifically, as demonstrated in Fig. 2D–F and S13 (ESI),† the low-frequency mode of T-NSD belonging to dihedral angles accounted for 48.19% of the total reorganization energy in sharp contrast to 22.44% of T-BTD, indicating the distinct conformation changes between the S_0 and the excited-state (S_1) with a root mean squared displacement value of 0.737 Å.[34] The PA spectra of T-NSD demonstrated its capacity for conducting PAI (Fig. S14, ESI†).

2.2 Preparation and characterization of T-NSD NPs

The feasibility of T-NSD for bioimaging was then verified by employing DSPE-$mPEG_{2000}$ as the encapsulation matrix to fabricate T-NSD NPs (Fig. 3A). As illustrated in Fig. 3B, the unified spherical shape of T-NSD NPs with an average diameter of approximately 114 nm and 65 nm was determined by dynamic light scattering (DLS) and transmission electron microscopy (TEM), respectively. After a storage period of 7 days, slight variations were observed in terms of the size of T-NSD NPs, demonstrating their excellent colloidal stability (Fig. S15,

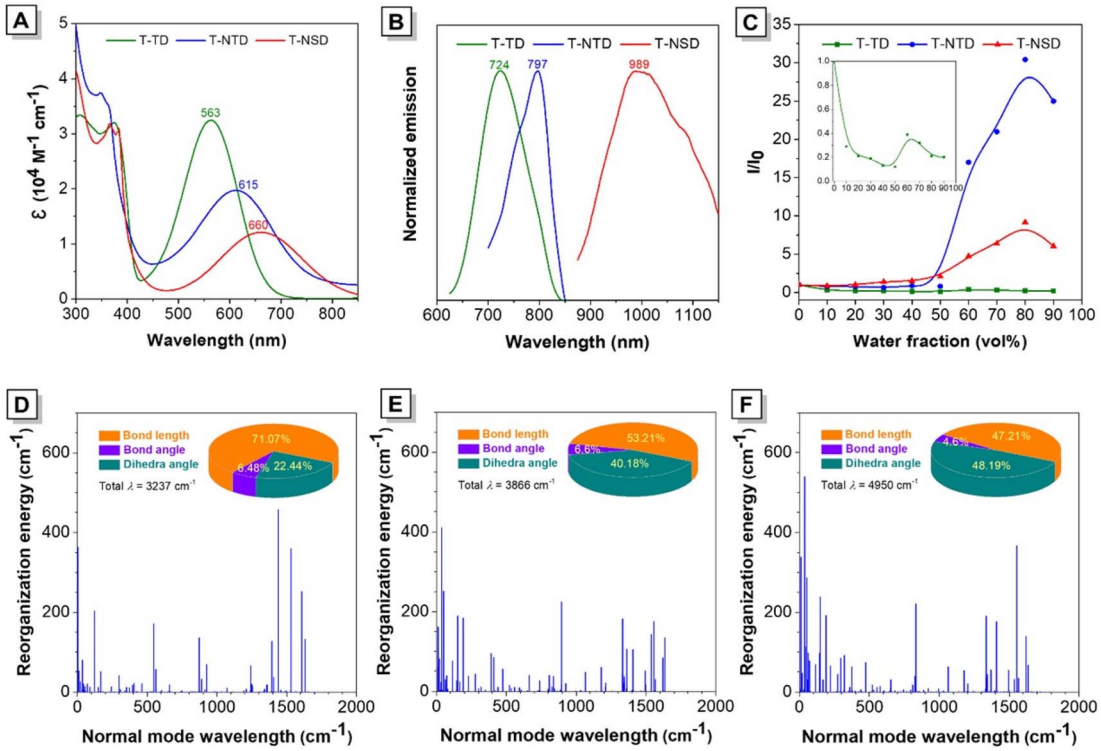

Fig. 2 Photophysical property study of T-BTD, T-NTD and T-NTD. (A) The absorption and (B) emission spectra of the obtained compounds dissolved in THF solution (10 μM, excited at 563 nm, 615 nm and 660 nm, respectively). (C) Plots of relative PL intensity (I/I_0) of the obtained compounds *versus* different water fractions. Inset: enlarged plot of T-BTD. I_0 and I are the values of PL intensities at maximum peaks in THF and THF/water mixtures, respectively. Calculated reorganization energy *versus* the normal mode wavenumbers of (D) T-BTD, (E) T-NTD, and (F) T-NSD, respectively.

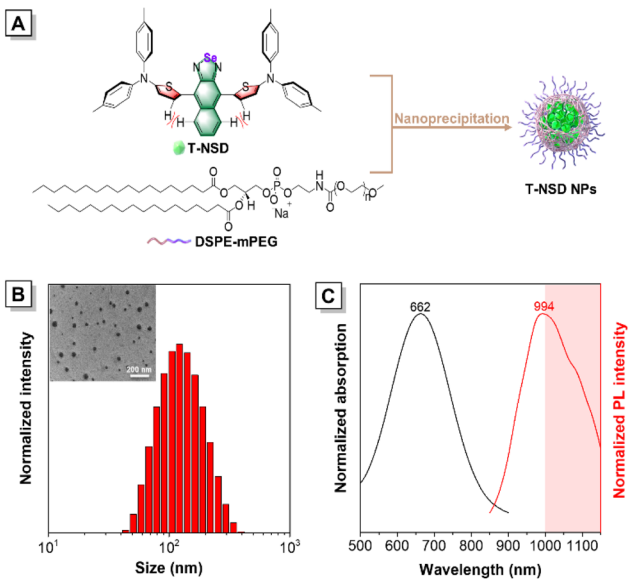

Fig. 3 Characterization of the T-NSD NPs. (A) The diagrammatic drawing of the fabrication process of T-NSD NPs. (B) DLS analysis of T-NSD NPs. Inset: corresponding TEM image of T-NSD NPs. (C) Normalized absorption and fluorescence spectra of T-NSD NPs in aqueous solution (10 μM).

ESI†). As anticipated, the absorption peak and the fluorescence emission peak were present at 662 nm and 994 nm, respectively, which is similar to those of its dilute THF solution. Noteworthily, the large Stokes shift (332 nm) of T-NSD NPs is advantageous for the implementation of NIR-II FLI (Fig. 3C). The good photostability of T-NSD NPs was further confirmed by minimal absorbance variations during continuous irradiation with a 660 nm laser at a power density of 0.1 W cm^{-1} (Fig. S16, ESI†). The relative quantum yield of T-NSD NPs was determined to be 0.15% by using indocyanine green as a reference (Fig. S17 and Table S1, ESI†).

2.3 *In vitro* cellular uptake experiments

The cytotoxicity of T-NSD NPs in living cells was evaluated by using CCK-8 and MTT assays to demonstrate their potential for bioimaging. The cell viability of HeLa cells incubated with varying concentrations of T-NSD NPs for 24 hours was initially examined, as depicted in Fig. 4A. The overall cell viability remained above 80%, despite a slight decrease observed at a concentration of 50 μg mL^{-1}. The minimal cytotoxicity of T-NSD NPs was further confirmed by quantitatively evaluating the viability of 4T1 tumor cells *via* the MTT assays (Fig. 4B). Taken together, these results demonstrated that T-NSD NPs possessed good biocompatibility and are well-suited for bioimaging.

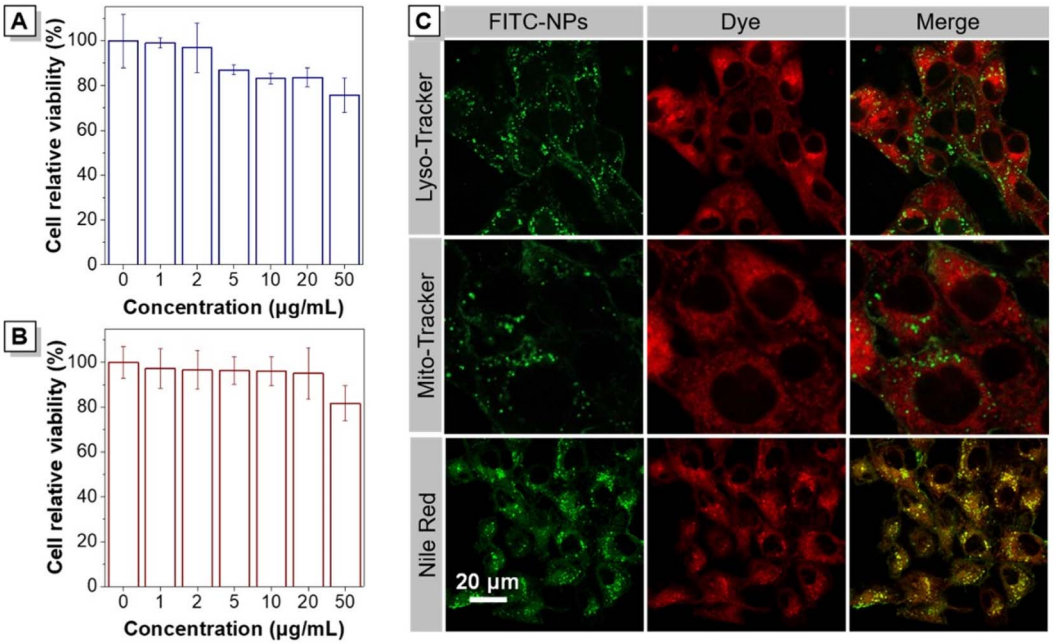

Fig. 4 The cytotoxicity and *in vitro* bioimaging study of T-NSD NPs. (A) HeLa cell and (B) 4T1 cell viabilities after staining with different concentrations of T-NSD NPs. (C) Co-localization test of FITC-NPs with Nile Red, Mito-Tracker, and Lyso-Tracker, respectively in 4T1 cells.

To better explore the intracellular uptake and distribution of T-NSD NPs in 4T1 cells, FITC-modified FITC-NPs were prepared by using FITC-DSPE-mPEG$_{2000}$ as the matrix. After incubation with FITC-NPs for 3 hours, 4T1 cells exhibited evident green fluorescence signals. With the incubation time prolonged to 12 h, a prominent fluorescence signal was distinctly observed, showcasing the efficient cellular internalization of FITC-NPs (Fig. S18, ESI†). To further investigate the intracellular localization in 4T1 cells, three commercially available probes, Nile Red, Mito-Tracker, and Lyso-Tracker, were employed to co-stain with the FITC-NPs. The fluorescence of FITC-NPs exhibited poor overlap efficiency with that of Mito-Tracker and Lyso-Tracker, as depicted in Fig. 4C. By comparison, the fluorescence signals of FITC-NPs and Nile Red exhibited a good overlap with a Pearson's value of 0.72, providing compelling evidence for the entry of FITC-NPs into lipid droplets.

2.4 *In vivo* dual-modal NIR-II FLI/PAI

The good biological safety of T-NSD NPs at the cellular level prompted us to assess their *in vivo* imaging performance. First, a 4T1 tumor-xenografted mouse model was established. To systematically study the *in vivo* distribution of T-NSD NPs and their optimal accumulation time in tumors, the fluorescence signal in tumor-bearing mice was investigated by using a NIR-II imaging system. As depicted in Fig. 5A, a negligible fluorescence signal was observed prior to the administration of T-NSD NPs, benefitting from the minimal tissue autofluorescence in the NIR-II region. Through tail-vein injection of T-NSD NPs, an obvious NIR-II fluorescence signal at the tumor sites was detected at 1 h post-injection originating from the enhanced permeability and retention effect.[35,36] The fluorescence intensity gradually increased with the prolongation of administration time and reached its maximum accumulation at 36 h post-injection (Fig. 5B). Of note, a strong fluorescence signal remained detectable even 168 h after injection, proving the long-term retention effect of T-NSD NPs within the tumors (Fig. S19, ESI†). The excellent tumor-accumulating capacity of T-NSD NPs was further confirmed by the *ex vivo* imaging of organs (Fig. S20, ESI†). We continuously performed PAI in the same 4T1 tumor-bearing mouse model. As shown in Fig. 5C and D, it is not surprising that the photoacoustic signals of the tumor area exhibited a gradual increase over time, reaching their maximum at 36 hours post-administration, which was consistent with the results obtained from NIR-II FLI. In summary, T-NSD NPs can be successfully employed for concurrent NIR-II FLI/PAI, demonstrating promising prospects for imaging-guided tumor resection.

2.5 Biocompatibility study of T-NSD NPs

The potential systemic cytotoxicity was then determined through comprehensive assessments. First, an *in vitro* hemolytic experiment was conducted in the presence of T-NSD NPs, demonstrating no signs of hemolysis even at a concentration as high as 100 μg mL^{-1} (Fig. 6A). Following this, T-NSD NPs were intravenously administered to mice, and blood samples were collected after one week for blood analysis. As demonstrated in Fig. 6B and Table S2 (ESI),† the parameters relating to routine blood, liver and kidney functions showed no discernible variations between the T-NSD NP group and the PBS group, illustrating that T-NSD NPs do not lead to any impairment of the normal physiological functions of mice. The influence of the T-NSD NPs on histopathological changes in major organs (heart,

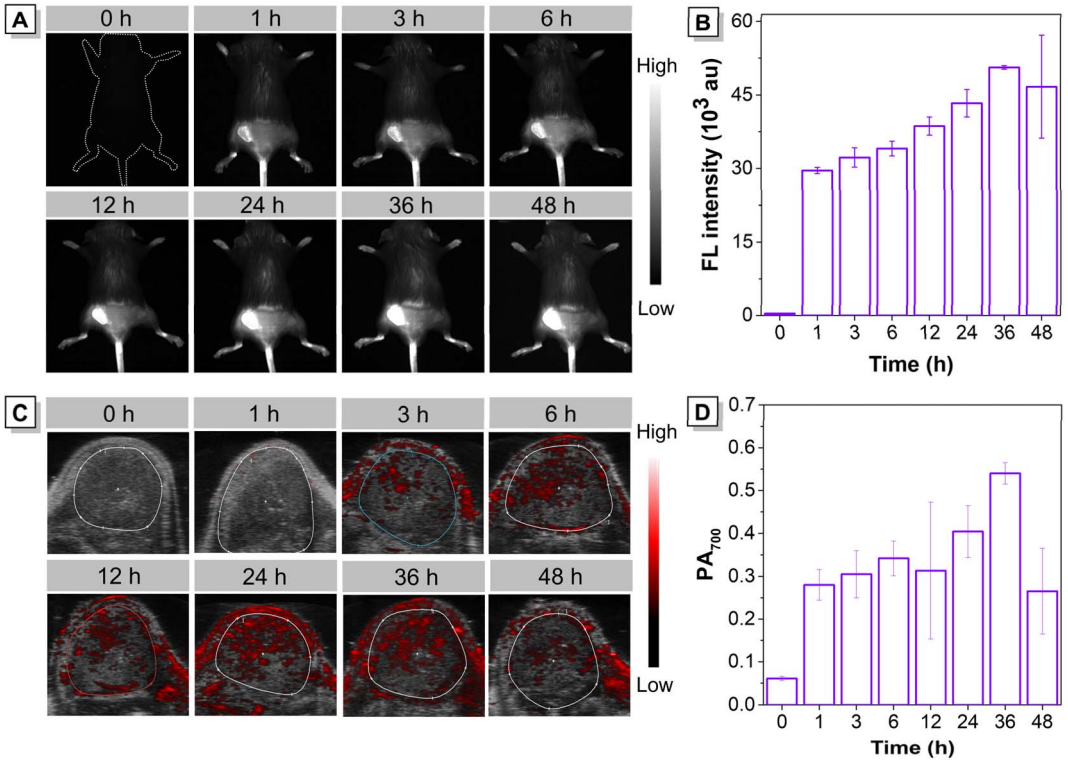

Fig. 5 *In vivo* NIR-II FLI and PAI. (A) NIR-II FLI on 4T1 tumor-bearing mice after injection of T-NSD NPs. (B) Corresponding average fluorescence intensity of tumor sites at different time points based on the images in (A) ($n = 3$). (C) PAI on 4T1 tumor-bearing mice after injection of T-NSD NPs (PA 700 nm). (D) The photoacoustic signal intensity within the solid coil at the tumor site based on the images in (C) ($n = 3$).

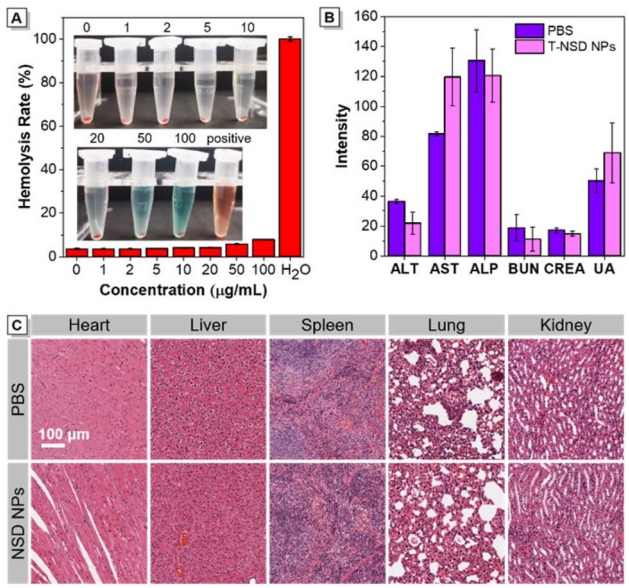

Fig. 6 The biosafety evaluation of T-NSD NPs ($n = 3$). (A) *In vitro* hemolysis experiments. (B) Liver function and kidney function indicators ($n = 3$). (C) H&E-stained photomicrographs of major organs.

liver, spleen, lung, and kidney) was assessed by H&E staining. From the results presented in Fig. 6C, the administration of T-NSD NPs for seven days did not result in any evident pathological abnormalities, manifesting minimal impact on organ function.

3 Conclusions

In this study, we have developed a novel NIR-II emissive molecule showing AIE characteristics for highly efficient bimodal tumor imaging. By tactfully manipulating the molecular acceptor, both a distorted structural conformation and promoted intermolecular charge transfer effect are simultaneously achieved to yield T-NSD through a facile synthetic protocol. After being fabricated into nanoparticles, T-NSD NPs exhibited remarkable NIR-II FLI/PAI ability with good colloidal stability. Furthermore, *in vitro* experiments validated the efficient cellular uptake of T-NSD NPs with minimal cytotoxicity. Eventually, *in vivo* dual-modal NIR-II FLI/PAI demonstrated the exceptional passive targeting capability and commendable biocompatibility of T-NSD NPs in a 4T1 tumor-xenografted mouse model. This work is believed to stimulate more endeavours in the development of high-performance NIR-II AIEgens for disease diagnosis.

Data availability

The authors confirm that the data supporting the findings of this study are available with the article [and/or its ESI†].

Author contributions

LX, DY, DW and BZT designed the research, LX, YT, JZ, WH and DY performed the research, LX, YT, JZ, WH, DY DW and BZT analyzed the data, and LX, DY, DW and BZT wrote the paper.

Conflicts of interest

There are no conflicts to declare.

Acknowledgements

This work was partially supported by the National Natural Science Foundation of China (52122317, 22175120, and 22307080), the Developmental Fund for Science and Technology of Shenzhen Government (RCYX20200714114525101), the Shenzhen Science and Technology Program (RCBS20221008093224016, JCYJ20220531101201003, and 20220809130438001), the Guangdong Basic and Applied Basic Research Fund (2023A1515010558), the Pearl River Talent Recruitment Program (2019QN01Y103), the Research Team Cultivation Program of Shenzhen University (2023QNT003), the Medical-Engineering Interdisciplinary Research Foundation of Shenzhen University (2023YG021), and the Medicine Plus Program of Shenzhen University (2024YG004). The authors also acknowledge HZWTECH for providing computation facilities and the Instrumental Analysis Center of Shenzhen University.

Notes and references

1 P. Zhang, W. Li, C. Liu, F. Qin, Y. Lu, M. Qin and Y. Hou, *Exploration*, 2023, **3**, 20230070.
2 P. Cheng and K. Pu, *Nat. Rev. Mater.*, 2021, **6**, 1095–1113.
3 X. Huang, J. Song, B. C. Yung, X. Huang, Y. Xiong and X. Chen, *Chem. Soc. Rev.*, 2018, **47**, 2873–2920.
4 Y. Chen, S. Wang and F. Zhang, *Nat. Rev. Bioeng.*, 2023, **1**, 60–78.
5 C. Li, G. Chen, Y. Zhang, F. Wu and Q. Wang, *J. Am. Chem. Soc.*, 2020, **142**, 14789–14804.
6 G. Hong, A. L. Antaris and H. Dai, *Nat. Biomed. Eng.*, 2017, **1**, 0010.
7 D. Yan, Y. Huang, J. Zhang, Q. Wu, G. Song, J. Ji, Q. Jin, D. Wang and B. Z. Tang, *J. Am. Chem. Soc.*, 2023, **145**, 25705–25715.
8 C. Xu and K. Pu, *Chem. Soc. Rev.*, 2021, **50**, 1111–1137.
9 X. Zhen, K. Pu and X. Jiang, *Small*, 2021, **17**, 2004723.
10 X. Liu, Y. Duan and B. Liu, *Aggregate*, 2021, **2**, 4–19.
11 J. Weber, P. C. Beard and S. E. Bohndiek, *Nat. Methods*, 2016, **13**, 639–650.
12 D. Yan, M. Wang, Q. Wu, N. Niu, M. Li, R. Song, J. Rao, M. Kang, Z. Zhang, F. Zhou, D. Wang and B. Z. Tang, *Angew. Chem., Int. Ed.*, 2022, **61**, e202202614.
13 S. Y. Ong, C. Zhang, X. Dong and S. Q. Yao, *Angew. Chem., Int. Ed.*, 2021, **60**, 17797–17809.
14 Q. Wang, Y. Dai, J. Xu, J. Cai, X. Niu, L. Zhang, R. Chen, Q. Shen, W. Huang and Q. Fan, *Adv. Funct. Mater.*, 2019, **29**, 1901480.
15 S. Song, Y. Zhao, M. Kang, F. Zhang, Q. Wu, N. Niu, H. Yang, H. Wen, S. Fu, X. Li, Z. Zhang, B. Z. Tang and D. Wang, *Adv. Mater.*, 2024, 2309748.
16 H. Li, Y. Kim, H. Jung, J. Y. Hyun and I. Shin, *Chem. Soc. Rev.*, 2022, **51**, 8957–9008.
17 S. Song, Y. Wang, Y. Zhao, W. Huang, F. Zhang, S. Zhu, Q. Wu, S. Fu, B. Z. Tang and D. Wang, *Matter*, 2022, **5**, 2847–2863.
18 C. Chen, H. Ou, R. Liu and D. Ding, *Adv. Mater.*, 2020, **32**, 1806331.
19 D. Yan, Y. Qin, S. Yan, P. Sun, Y. Wang, D. Wang and B. Z. Tang, *Particuology*, 2023, **74**, 103–118.
20 W. Z. Yuan, P. Lu, S. M. Chen, J. W. Y. Lam, Z. M. Wang, Y. Liu, H. S. Kwok, Y. G. Ma and B. Z. Tang, *Adv. Mater.*, 2010, **22**, 2159–2163.
21 M. Kang, Z. Zhang, N. Song, M. Li, P. Sun, X. Chen, D. Wang and B. Z. Tang, *Aggregate*, 2020, **1**, 80–106.
22 B. Li, W. Wang, L. Zhao, M. Li, D. Yan, X. Li, J. Zhang, Q. Gao, Y. Feng, J. Zheng, B. Shu, Y. Yan, J. Wang, H. Wang, L. He, Y. Wu, S. Zhou, X. Qin, W. Chen, K. Qiu, C. Shen, D. Wang, B. Z. Tang and Y. Liao, *Adv. Mater.*, 2023, 2305378.
23 D. Li, X. Chen, W. Dai, Q. Jin, D. Wang, J. Ji and B. Z. Tang, *Adv. Mater.*, 2023, 2306476.
24 S. Yang, J. Zhang, Z. Zhang, R. Zhang, X. Ou, W. Xu, M. Kang, X. Li, D. Yan, R. T. K. Kwok, J. Sun, J. W. Y. Lam, D. Wang and B. Z. Tang, *J. Am. Chem. Soc.*, 2023, **145**, 22776–22787.
25 D. Yan, T. Li, Y. Yang, N. Niu, D. Wang, J. Ge, L. Wang, R. Zhang, D. Wang and B. Z. Tang, *Adv. Mater.*, 2022, **34**, 2206643.
26 P. Xiao, W. Xie, J. Zhang, Q. Wu, Z. Shen, C. Guo, Y. Wu, F. Wang, B. Z. Tang and D. Wang, *J. Am. Chem. Soc.*, 2023, **145**, 334–344.
27 D. Yan, W. Xie, J. Zhang, L. Wang, D. Wang and B. Z. Tang, *Angew. Chem., Int. Ed.*, 2021, **60**, 26769–26776.
28 W. Xu, D. Wang and B. Z. Tang, *Angew. Chem., Int. Ed.*, 2021, **60**, 7476–7487.
29 Y. Tan, Y. Sun, W. Huang, D. Zhu, D. Yan, D. Wang and B. Z. Tang, *Luminescence*, 2024, **39**, e4606.
30 J. Xue, Q. Liang, Y. Zhang, R. Zhang, L. Duan and J. Qiao, *Adv. Funct. Mater.*, 2017, **27**, 1703283.
31 Z. Shuai, *Chin. J. Chem.*, 2020, **38**, 1223–1232.
32 Z. Shuai and Q. Peng, *Phys. Rep.*, 2014, **537**, 123–156.
33 Z. Shuai and Q. Peng, *Natl. Sci. Rev.*, 2017, **4**, 224–239.
34 S. Liu, C. Chen, Y. Li, H. Zhang, J. Liu, R. Wang, S. T. H. Wong, J. W. Y. Lam, D. Ding and B. Z. Tang, *Adv. Funct. Mater.*, 2019, **30**, 1908125.
35 R. Sun, J. J. Xiang, Q. Zhou, Y. Piao, J. B. Tang, S. Q. Shao, Z. X. Zhou, Y. H. Bae and Y. Q. Shen, *Adv. Drug Delivery Rev.*, 2022, **191**, 114614.
36 E. A. Azzopardi, E. L. Ferguson and D. W. Thomas, *J. Antimicrob. Chemother.*, 2013, **68**, 257–274.